Journal of Materials Chemistry C

Accepted Manuscript

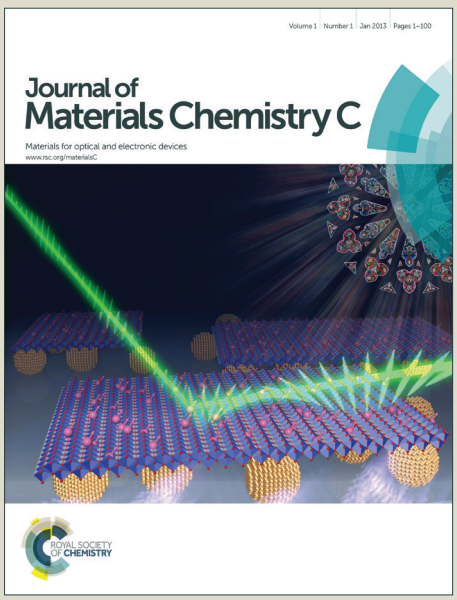

ROYAL SOCIETY OF CHEMISTRY

www.rsc.org/materialsC

Controlled synthesis and tunable luminescence of uniform $YPO_4 \cdot 0.8H_2O$ and $YPO_4 \cdot 0.8H_2O$:Tb^{3+}/Eu^{3+} nanocrystals by a facile approach

Lei Zhang [a], Linlin Fu [a], Xingxing Yang [a], Zuoling Fu [a, *], Xiangdong Qi[c], Zhijian Wu[b]

[a] *State Key Laboratory of Super-hard Materials, College of Physics, Jilin University, Changchun 130012, China*

[b] *State Key Laboratory of Rare Earth Resources Utilization, Changchun Institute of Applied Chemistry, Chinese Academy of Sciences, Changchun 130022, China*

[c] *Changchun Institute of Optics, Fine Mechanics and Physics, Chinese Academy of Sciences, Changchun 130033, China*

E-mail: zlfu@jlu.edu.cn (Z. L. Fu)

Telephone: 86-431-85167966

Fax: 86-431-85167966

Abstract

Uniform and well-crystallized $YPO_4 \cdot 0.8H_2O$ and $YPO_4 \cdot 0.8H_2O$:Tb^{3+}, Eu^{3+} nanocrystals have been successfully synthesized by a facile hydrothermal method using trisodium citrate (Cit^{3-}) as a "shape modifier". X-ray diffraction (XRD), field emission-scanning electron microscopy (FE-SEM), high-resolution transmission electron microscopy (HRTEM) and photoluminescence (PL) spectra were used to characterize the samples. It was found that the pH value in the initial solution was responsible for shape determination of final products. In addition, the $YPO_4 \cdot 0.8H_2O$ samples prepared by Cit^{3-}-assisted hydrothermal synthesis exhibited an intense and bright blue emission. Characterized with Fourier transform infrared (FT-IR) spectra and Electron paramagnetic resonance (EPR) spectra, the carbon-related impurities induced by trisodium citrate (Cit^{3-}) in the hydrothermal process were confirmed and proved that the paramagnetic defects relating to the luminescence property existed in the luminescent $YPO_4 \cdot 0.8H_2O$ nanocrystals. More interesting was that the $YPO_4 \cdot 0.8H_2O$:Tb^{3+}, Eu^{3+} samples could be effectively excited with 380 nm and the luminescence colors of $YPO_4 \cdot 0.8H_2O$: Tb^{3+}, Eu^{3+} nanocrystals can be easily tuned by changing the concentration of Eu^{3+} ions due to an efficient energy transfer from Tb^{3+} to Eu^{3+}. These results revealed that the combination of the defect luminescence and rare earth-doping emission in $YPO_4 \cdot 0.8H_2O$: Tb^{3+}, Eu^{3+} nanocrystals could result in tunable emission in a large color gamut, which may be potentially applied in fields such as solid state lighting and field emission displays.

Keywords: Nanocrystals; Hydrothermal synthesis; Defect luminescence; Tunable

luminescence

1. Introduction

In recent years, inorganic luminescent materials/phosphors are playing a key role in applications of lighting (e.g., fluorescent tubes and LEDs), displays (e.g., cathode tube display and field emission display), imaging (computed tomography), etc. [1−4] The current attention on energy savings and green issues gives a boost to the development of LEDs for lighting, due to their advantages of high efficiency, compactness, long operational lifetime, and environmental friendliness.[2,3] Rare earth luminescent materials have attracted much attention of scientists due to their unique electronic, optical, and chemical properties resulted from the 4f shell of the ions and were extensively applied to high-performance magnets, luminescence devices, displays, biolabeling, optical imaging, or phototherapy, etc.[4,5] It is well known that the intrinsic properties of inorganic materials are determined by their sizes, shapes, morphologies, compositions, and crystallinity.[6,7] Thus, further explorations of well-controlled shapes and novel structures of inorganic rare earth luminescent materials have become an important research subject faced by synthetic inorganic chemists.

To date, great efforts have been devoted to design inorganic nanomaterials with well-defined sizes, shapes, and crystallinity, such as lanthanide hydroxide nanowires/nanorods, nanotubes, nanosheets,[8-11] lanthanide orthophosphate nanocrystals,[12-15] nanowires/nanorods[16-19] and nanofibers.[20] Nowadays, it is widely accepted that one of the promising and popular strategies of shape and size control is

to select carefully an appropriate organic additive with functional groups that selectively adhere to a particular crystal facet and lead to the morphological modification of the crystals.[21] Among a variety of organic additives, trisodium citrate (labeled as Cit^{3-}) is one of the most common and important organic molecules that has been used extensively as the stabilizer and structure-directing agent to control the nucleation, growth and alignment of crystals.[22,23] For instances, Qian and coworkers reported the influences of Cit^{3-} on the Co nanowires[24] and doughnut-shaped ZnO microparticles.[25] Moreover, the trisodium citrate has effects on the luminescence of materials except the "shape modifier".

$LnPO_4$ (Ln=Y, La, Gd, Lu) has high thermal and chemical stability[26] because the mentioned Ln^{3+} has an empty or half-filled or fully filled 4f electron shell with stable structure. $LnPO_4$ (Ln^{3+} = Y, La, Gd, Lu) is suggested to be an excellent host for luminescent materials. In recent years, the compounds $LnPO_4$ (Ln = Y, La, Gd, Lu) have been largely investigated.[16-18] Hasse and co-workers obtained $LnPO_4$ nanocrystals dispersions with good optical properties using a surfactant-assisted route.[27] Feldmann and coworker synthesized luminescent $LaPO_4:Ce^{3+},Tb^{3+}$ nanoparticles with a high quantum yield using a microwave-assisted synthesis method with ionic liquids as the reaction media.[28] However, there are still few reports on the synthesis and luminescent properties of $YPO_4 \cdot 0.8H_2O$ nanocrystals. In this work, we chose to synthesize Tb^{3+}/Eu^{3+}-doped $YPO_4 \cdot 0.8H_2O$ nanocrystals for two specific reasons. On the one hand, we attempted to control the size, morphology, and crystallinity of $YPO_4 \cdot 0.8H_2O$ nanocrystals by use of an organic additive (Cit^{3-}) via

the hydrothermal process and try to analysis the mechanism of the luminescence. On the other hand, Tb^{3+} and Eu^{3+} in some crystalline modifications of orthophosphates were themselves excellent green and red light emitting centers, respectively. The luminescent properties of Eu^{3+}, Tb^{3+}-codoped $YPO_4 \cdot 0.8H_2O$ phosphors were investigated in detail and energy transfer mechanism between rare earth ions was also discussed.

2. Experimental details

2.1. Preparation of Eu^{3+}/Tb^{3+}-doped $YPO_4 \cdot 0.8H_2O$ Nanocrystals

Materials. Lanthanum oxide, terbium oxide and europium oxide (all 99.99%) were used as the starting raw materials. All other chemicals used were analytical grade without further purification. Rare earth nitrate ($Tb(NO_3)_3$ and $Eu(NO_3)_3$) stock solutions of 0.1 M and 0.2 M were prepared by dissolving Eu_2O_3 and Tb_4O_7 in concentrated HNO_3 at elevated temperature. The yttrium nitrate hexahydrate ($Y(NO_3)_3 \cdot 6H_2O$) and sodium phosphate (Na_3PO_4) were used as the yttrium source and phosphate source, respectively. Meanwhile, trisodium citrate (A. R.) was used as the "shape modifier".

Synthesis. In a typical procedure, 2mmol $Y(NO_3)_3 \cdot 6H_2O$ was added to the 20 mL of the aqueous solution containing the 2mmol of trisodium citrate (Cit^{3-}) to form the Y^{3+}-Cit^{3-} complex (1:1 molar ratio for Cit^{3-}/Y^{3+}). After vigorous stirring for 30 min, 2 mmol of Na_3PO_4 was added into the above solution. The pH of the mixture was adjusted to a specific value by adding NaOH solution (3M) or HNO_3 (1M) solution. After additional agitation for 15 min, the as-obtained mixing solution was transferred

into a Teflon bottle held in a stainless steel autoclave, sealed and maintained at 180 ℃ for 24 h. As the autoclave was cooled to room temperature naturally, the precipitates were separated by centrifugation, washed with deionized water and ethanol in sequence, and then dried in air at 60 °C for 12 h. Finally, the uniform distribution spherical $Y_{0.96}PO_4 \cdot 0.8H_2O$: $0.04Tb^{3+}$ nanocrystals were obtained. The experiment was repeated at similar conditions for the synthesis of $Y_{(0.96-x)}$ $PO_4 \cdot 0.8H_2O$: 0.04 Tb^{3+}, x Eu^{3+}.

2.2. Characterization

X-ray powder diffraction (XRD) measurements were performed on a Rigaku-Dmax 2500 diffractometer at a scanning rate of 15 °/min in the 2θ range from 10° to 65°, with graphite monochromatized Cu Kα radiation (λ = 0.15405 nm). The morphology and size of the obtained samples were examined by a field emission-scanning electron microscope (FE-SEM, XL30, Philips) and high-resolution transmission electron microscopy (HR-TEM). The ultraviolet-visible photoluminescence (PL) excitation and emission spectra were recorded with a Hitachi F-7000 spectrophotometer equipped with Xe-lamp as an excitation source. Fourier transform infrared (FT-IR) spectrum was obtained with a Perkin-Elmer 580B infrared spectrophotometer with the KBr pellet technique. Electron paramagnetic resonance (EPR) spectra were obtained on a JES-FA 200 EPR spectrometer. The luminescent dynamics were investigated using a three part laser system consisting of a (i) Nd:YAG pumping laser (1064 nm), (ii) third-order harmonic generator (blue laser at 486 nm), and (iii) tunable optical parametric oscillator (OPO, Continuum Precision II 8000);

with a pulse duration of 10 ns, repetition frequency of 10 Hz, and line width of 4–7 cm^{-1}. All the measurements were performed at room temperature.

3. Results and Discussion

3.1. Phase Identification and Morphologies

The composition and phase purity of the as-prepared powder samples were first examined by XRD. Different pH values for the synthesis of single phase $YPO_4 \cdot 0.8H_2O$ nanocrystals were investigated by varying the base or acid (NaOH or HNO_3) concentration used in the reaction system. Figure 1 (a)-(g) presented the XRD patterns of prepared $YPO_4 \cdot 0.8H_2O$ samples at different pH vales from 6 to 12, respectively. And it can be observed that no impurity lines were observed and all the diffraction peaks can be indexed to the pure hexagonal phase of hydrated YPO_4 samples. Figure 2 showed representative X-ray diffraction patterns of the $YPO_4 \cdot 0.8H_2O$ (a); $YPO_4 \cdot 0.8H_2O$: Tb^{3+} (b) ; $YPO_4 \cdot 0.8H_2O$: Eu^{3+} (c); $YPO_4 \cdot 0.8H_2O$: Eu^{3+}, Tb^{3+} (d) samples, respectively. All the diffraction peaks can be readily indexed to pure hexagonal phase according to the JCPDS file No. 42-0028. No obvious shifting of peaks or second phase can be detected at current doping level, indicating that the Tb^{3+} and Eu^{3+} ions were completely dissolved in the $YPO_4 \cdot 0.8H_2O$ host lattice by substituting for the Y^{3+}. It is also observed that the XRD patterns in Figure 2(b)-(d) shows broad diffraction peaks, so that $YPO_4 \cdot 0.8H_2O$: Eu^{3+}, Tb^{3+} particles with nanometer size are expected to form.

The FE-SEM and TEM images provide direct information about the size and typical shapes of the as-synthesized $YPO_4 \cdot 0.8H_2O$ samples grown under different

experimental conditions. Figure 3 illustrated the representative FE-SEM and TEM images of the samples prepared at different pH values. The representative panoramic FE-SEM images shown in Figure 3 (a) and (b) demonstrated that the product was composed of a great deal of hexagonal nanoprisms with 120 nm in diameter and 130 nm in length at pH=6, respectively. Moreover, the hexagonal nanoprisms were uniform distribution, the crystallographic facets were very smooth and clear. When the pH value of the initial solution was increased to 11 adjusted with NaOH (3 M), the spherical-like nanoparticles were produced as shown in Figure 3(c) and 3(d). However, we can see that the well-defined crystallographic facets of hexagonal prisms were not very evident and a small quantity of spherical-like particles can also be observed. Furthermore, the surfaces of crystals were very coarse with some smaller nanoparticles attached on them. These results powerfully demonstrated that the different pH values of the precursor showed a large impact on the morphologies and nanostructures of $YPO_4 \cdot 0.8H_2O$, and increase of the pH value will make the particles become uneven. Therefore, a crystallization pH value of 6 was optimal. What is more, it is reasonable to show the TEM and HR-TEM images at pH=6 in the Figure 3(e) and Figure 3(f). From Figure 3(e), regular hexagonal cross-section can be seen that corresponded to individual hexagonal prism lying flat on the bottom face parallel to the substrate. The HR-TEM image (Figure 3(f)) showed that the as-obtained crystals were highly crystalline and that the lattice spacing was determined as ~0.60 nm.

3.2 Luminescence of $YPO_4 \cdot 0.8H_2O$ Nanocrystals

Under UV-light irradiation, the $YPO_4 \cdot 0.8H_2O$ nanocrystals exhibited a strong blue emission. Figure 4 showed the excitation and emission spectra of as-prepared $YPO_4 \cdot 0.8H_2O$ in the synthesis process. From Figure 4, we can see that the $YPO_4 \cdot 0.8H_2O$ with Cit^{3-} sample showed a strong emission consisting of a broad band (380-500 nm) with a maximum at 400 nm, and the corresponding excitation spectrum included two broad bands: a weak band from 200 to 240 nm and a strong broad band from 320 to 400 nm with a maximum at 369 nm. In addition, the control experiment without Cit^{3-} in the preparation was also performed. The as-obtained $YPO_4 \cdot 0.8H_2O$ sample in the absence of **Cit^{3-}** showed no luminescence just the dashed line presented in Figure 4, indicating that the trisodium citrate was the key factor causing the blue luminescence. Since neither the Y^{3+} nor the PO_4^{3-} group is able to show luminescence,[29, 30] the only difference in the hydrothermal process between the luminescent samples and non-luminescent samples is that the former has trisodium citrate as additives while the latter does not, therefore the observed blue luminescence from $YPO_4 \cdot 0.8H_2O$ sample may be related to some impurities and/or defects in the host lattice. In order to explore the luminescent mechanism, EPR spectroscopy on the luminescent $YPO_4 \cdot 0.8H_2O$ nanocrystals with and without the Cit^{3-} were performed (Figure 5). It can be observed that the luminescent $YPO_4 \cdot 0.8H_2O$ sample (Figure 5a) showed two obvious EPR signals at g=2.0000 and g=2.0066, but the $YPO_4 \cdot 0.8H_2O$ sample prepared without Cit^{3-} exhibited no EPR signal in Figure 5b. This indicated that the paramagnetic defects relating to the luminescence property existed in the luminescent $YPO_4 \cdot 0.8H_2O$ nanocrystals, which was in agreement with the similar

situation reported by Angelov et al.,[31] who found that the $CO_2^{\cdot-}$ radicals exhibiting three EPR signals in the interstitial sites of the aragonite lattice of $SrCO_3$ were most probably responsible for the self-activated luminescence. In addition, Lin Jun's group has reported the luminescence properties of $CO_2^{\cdot-}$ radicals in $Ca_5(PO_4)_3OH$ and $Sr_5(PO_4)_3OH$ host lattice without doping rare earth or transition metal ions as activators.[32,33] Compared with the present work, EPR signal, the similar PL results, together with the synthesis process, we can assume that the luminescence for $YPO_4 \cdot 0.8H_2O$ nanocrystals might be induced by $CO_2^{\cdot-}$ radicals in the $YPO_4 \cdot 0.8H_2O$ host lattice. The $CO_2^{\cdot-}$ radicals might be formed from Cit^{3-} in the hydrothermal process. These radicals may become optically active centers of self-activated orthophosphate luminescence. In the preparation of orthophosphate samples via the hydrothermal process with Cit^{3-}, it is easy to form the metal-citrate complex. Under the high pressure and thermal process, some of R-C-COO- (Cit^{3-}) occurs bond cleavages to form R-C (big group) and $CO_2^{\cdot-}$, small amounts of $CO_2^{\cdot-}$ radicals resulting from the bond cleavages are trapped by the already formed orthophosphate lattice or interstitial positions. The residual fragmented bonds ($CO_2^{\cdot-}$) are apparently the precursors for various centers. These defects centers induce an electron being localized in 2p orbital of the single bonded carbon. This would give rise to photoluminescence through a strong electron-photon coupling.[34-36] To further confirm the presence of $CO_2^{\cdot-}$ radical impurities, the $YPO_4 \cdot 0.8H_2O$ samples were subjected to FT-IR analysis. The FT-IR spectra for $YPO_4 \cdot 0.8H_2O$ with Cit^{3-} (a) and $YPO_4 \cdot 0.8H_2O$ without Cit^{3-} (b) were shown in Figure 6. As shown in Figure 6a for the as-prepared $YPO_4 \cdot 0.8H_2O$ sample

in the presence of Cit^{3-}, the broadband at 3500cm^{-1} was ascribed to the O–H vibration of H_2O absorbed in the sample. The 1405 and 1618 cm^{-1} peaks were attributed to the carbon-related impurities from the addition of Cit^{3-} ions. The band centered at 1010 cm^{-1} was ascribed to the asymmetric stretching vibrations of the P–O in PO_4^{3-} groups. The two groups of bands in the low wavenumber ranging from 500 to 680 cm^{-1} (centered at 537, 624 cm^{-1}) were assigned to the bending vibrations of the O–P–O in PO_4^{3-} groups.[37-39] The FT-IR spectrum (Figure 6b) of $YPO_4 \cdot 0.8H_2O$ in the absence of Cit^{3-} in the synthesis process was similar to the spectrum of $YPO_4 \cdot 0.8H_2O$ with Cit^{3-} except that the intensity of the two bands (1405 and 1618 cm^{-1}). The two weak bands can be attributed to tiny amount of CO_2^{-} groups, which might be from the CO_2 in aqueous solution or air in the preparation process.[40-42] Through the analysis of the above experiment results, we can conclude that the radical defects were induced by Cit^{3-} in the hydrothermal process. The EPR and FT-IR results provided abundant evidence that the carbon-related impurities were induced by Cit^{3-} in the hydrothermal process.

3.3 Photoluminescence Properties of $YPO_4 \cdot 0.8H_2O$: Tb^{3+}/ Eu^{3+} nanocrystals

Eu^{3+} ion is a well-known red-emitting activator in commercial phosphors because the emission of the rare earth Eu^{3+} ion consists usually of lines in the red spectral area due to the $^5D_0$–^7F_J (J = 1, 2, 3, 4, 5 and 6) transitions. While the Tb^{3+} ion is used as an activator in green phosphors, whose emission is mainly due to transitions of $^5D_3 \rightarrow {}^7F_J$ in the blue region and $^5D_4 \rightarrow {}^7F_J$ in the green region (J = 6, 5, 4, 3, 2) depending on its doping concentration. In order to show the tunable luminescence, we can

co-dope different rare earth ions by variation of their concentration. In our experiment, we added into Tb^{3+} and Eu^{3+} ions in $YPO_4 \cdot 0.8H_2O$ nanocrystals.

Figure 7 depicts the excitation and emission spectra of $YPO_4 \cdot 0.8H_2O$: $0.04Tb^{3+}$ nanocrystals in the 200-700 nm range. The excitation spectrum (red line) consists of several broad bands. For comparison, the overall excitation spectrum is divided into two parts: one, in the range from 200-290nm, represents the 4f-5d transition of Tb^{3+}; the other, in the range from 290-400nm, represents the 4f-4f transition of Tb^{3+}. The former is assigned to the transitions from the lower energy level of the $4f^8$ configuration to the energy levels of the $4f^75d$ configuration of the Tb^{3+}, resulting in a direct excitation into Tb^{3+}. For the latter, as expected, this spectral shift is not observed, since the 4f shell of Tb^{3+} is well-shielded by 5s and 5p shells, resulting in little effect of crystal field on the energy levels. The characteristic f→f transition lines within the Tb^{3+} $4f^8$ configuration in the longer wavelength region are assigned as the transitions from the $^7F_6$ ground state to the different excited states of Tb^{3+}, that is, 353 nm ($^7F_6 \rightarrow {}^5D_2$), 360 nm ($^7F_6 \rightarrow {}^5L_{10}$), 371 nm ($^7F_6 \rightarrow {}^5G_5$), 379 nm ($^7F_6 \rightarrow {}^5G_6$), respectively.[43-45] Excitation into the $4f^8$-$4f^75d$ transition band yields the emission spectrum (black line) that has similar profiles and exhibits four obvious lines centered at 492, 545, 586, and 622 nm, originating from the transitions from the $^5D_4$ excited state to the ^7F_J (J=6, 5, 4, 3) ground states of Tb^{3+} ion respectively, with $^5D_4 \rightarrow {}^7F_5$ transition at 545 nm as the most prominent group.

Generally, the luminescence color of Eu^{3+} ion depends on the host structure, which mainly shows the characteristic emissions resulting from the transitions of the $^5D_{0,1,2}$

$\rightarrow {}^7F_J$ (J = 1, 2, 3, 4). [46] As shown in Figure 8, the excitation spectrum monitored with 592 nm consists of two broad excitation bands from 200-340 nm with a maximum at 218 nm, which should be ascribed to the host absorption and the charge transfer transition between O^{2-} and Eu^{3+}, respectively.[47] In the longer wavelength region (360-500 nm), Eu^{3+} doped phosphors usually have effective and intrinsic absorption due to the intra-configurational 4f-4f transition of Eu^{3+} at about 395 nm ($^7F_0 \rightarrow {}^5L_6$) and 465 nm ($^7F_0 \rightarrow {}^5D_2$), which make them match well with the near-UV and blue GaN-based LED chips as an efficient red light emitting phosphor. The emission spectrum (Figure 8, black line) is obtained under 395 nm excitation, which describes by the characteristic emission peaks of the Eu^{3+} ions with the transitions from the excited $^5D_0$ state to ^7F_J (J=1, 2) levels at about 592 and 614 nm, respectively. The emission at 592 nm is stronger than that of 614 nm, suggesting a higher occupancy of Eu^{3+} in the asymmetric environment.

3.4 Photoluminescence Properties of $YPO_4 \cdot 0.8H_2O$: Tb^{3+}, Eu^{3+} nanocrystals

Energy transfer plays an important role in improving the emission efficiency for solid-state luminescent materials. Since the whole rare earth family is isostructural, it is expected that we can easily tune their emissions by codoping methods. Among the lanthanide ions, the Eu^{3+} and Tb^{3+} ions are two of the most important luminescent activators, which are attractive in visible luminescent materials owing to their strong red and green emissions. So we can make them co-crystallize with tunable optical activity.[48,49] In addition, Eu^{3+} and Tb^{3+} have the same charge and similar ionic radii, hence Eu^{3+} can dope easily into the Tb^{3+} compounds and the corresponding emission

color tuning is decided according to the concentration of the Eu^{3+} ions through the energy-transfer process.[50] Therefore, Tb^{3+} and Eu^{3+} ions co-doped $YPO_4 \cdot 0.8H_2O$ nanocrystals was also prepared in our work and the emission spectrum of $YPO_4 \cdot 0.8H_2O$: $0.04Tb^{3+}$, $0.06Eu^{3+}$ nanocrystals was shown in Figure 9. Under the excitation at 380 nm, the red (614 nm, Eu^{3+}), green (545 nm, Tb^{3+}) and blue (494 nm, Tb^{3+}) emission bands can be excited concurrently besides defects/impurities broad band luminescence in the host. In addition, it can also be seen in Figure 10 that there is overlapping between the emission spectrum of Tb^{3+} and the excitation spectrum of Eu^{3+}. Therefore, we can speculate that there exists energy transfer among Tb^{3+} and Eu^{3+} ions in the $YPO_4 \cdot 0.8H_2O$ nanocrystals.[51-53] Besides, when exciting with 486 nm laser light corresponding to Tb^{3+}: $^7F_6 \rightarrow {}^5D_4$ transition (Figure 11), it can be observed that the emission spectrum (red line) simultaneously contains the 596nm ($^5D_0 \rightarrow {}^7F_1$) and 618nm ($^5D_0 \rightarrow {}^7F_2$) of Eu^{3+} and the 549nm ($^5D_4 \rightarrow {}^7F_5$) transition of Tb^{3+} in $YPO_4 \cdot 0.8H_2O$: $0.04Tb^{3+}$, $0.04Eu^{3+}$ nanocrystals, and the emission intensity of Tb^{3+} $^5D_4 \rightarrow {}^7F_5$ transition obviously decreases compared with that of Tb^{3+} $^5D_4 \rightarrow {}^7F_5$ transition in single $0.04Tb^{3+}$-doped $YPO_4 \cdot 0.8H_2O$ and $YPO_4 \cdot 0.8H_2O$: $0.04Tb^{3+}$, $0.02Eu^{3+}$ samples. Besides, the emission intensity of Eu^{3+} $^5D_0 \rightarrow {}^7F_2$ and $^5D_0 \rightarrow {}^7F_4$ transitions in $YPO_4 \cdot 0.8H_2O$: $0.04Tb^{3+}$, $0.04Eu^{3+}$ obviously increases compared with that of in $YPO_4 \cdot 0.8H_2O$: $0.04Tb^{3+}$, $0.02Eu^{3+}$ samples. All of the spectral results illustrate that Tb^{3+} ions may act as an energy donor in the $YPO_4 \cdot 0.8H_2O$ host, in which excitation energy could be transferred to an acceptor Eu^{3+}.

3.5 Energy Transfer and Luminescence Mechanism in $YPO_4 \cdot 0.8H_2O$: Tb^{3+},

Eu^{3+} Nanocrystals

Furthermore, to explore the possibility of the energy transfer and realize the multicolor tunable luminescence, Figure 12 shows the variation of PL spectra and emission intensity of $YPO_4 \cdot 0.8H_2O$: $0.04Tb^{3+}$, xEu^{3+} nanocrystals with the increase of Eu^{3+}-doping concentrations from 0 to 0.18, respectively. The sample (x=0) exhibits the typical emission of Tb^{3+} and is characterized by strong bands at ~545 nm ($^5D_4 \rightarrow {}^7F_3$ transition, green emission) and ~491 nm ($^5D_4 \rightarrow {}^7F_4$ transition, blue emission). Although the concentration of Tb^{3+} was fixed, the emission intensity of Tb^{3+} decreased with increasing Eu^{3+} concentration. While the emission intensity of Eu^{3+} firstly increases with the increasing of its concentration (x), reaching a maximum value at x=0.06, then decreases with further increasing (x) due to the concentration quenching effect. In many cases, concentration quenching is due to energy transfer from one activator to another until an energy sink in the lattice is reached. In the energy migration process the excitation energy will be lost at a killer or quenching site, resulting in the decrease of luminescence intensity. Moreover, as the ion radius of Eu^{3+} and Y^{3+} are different, the crystal structure distortion becomes more serious with an increase in the Eu^{3+} doping concentration, which would quench the luminescence. However, the luminescence intensity of the Eu^{3+} ions is not as expected, we speculate that there may be energy transfer between the host and the Eu^{3+} ions. After that, we made a series of experiments about doping the different rare earth ions, the spectral results are shown in Figure S1, which reveal that the change of the luminescent intensity could be related to the type of the rare earth ions. When La^{3+} ions without

luminescence are doped in $YPO_4 \cdot 0.8H_2O$ nanocrystals, the intensity of defects/impurities broad band luminescence in the host will be more stronger. When Tb^{3+} ions are doped in $YPO_4 \cdot 0.8H_2O$ nanocrystals, the intensity of defects/impurities broad band luminescence remains unchanged. However, the defects luminescence becomes weaker when Eu^{3+} ions are doped. Therefore, it is possible that there exists energy transfer between the defects in the host and the Eu^{3+} ions. Further experiments are under way.

In order to further validate the energy transfer from Tb^{3+} to Eu^{3+}, we investigated the decay curve of Tb^{3+}. As described by Blasse,[54] the decay behavior of Tb^{3+} can be expressed as

$$I = I_0 \exp(-t/\tau) \quad (1)$$

where I and I_0 are the luminescence intensities at time t and 0, and τ is the luminescence lifetime. Figure 13 shows the decay curves of Tb^{3+} emission in $YPO_4 \cdot 0.8H_2O$: $0.04Tb^{3+}$, xEu^{3+} (x=0, 0.02, 0.04, 0.06, 0.08, 0.10, 0.12, 0.14, 0.16, 0.18) samples. For the $YPO_4 \cdot 0.8H_2O$: 0.04 Tb^{3+}, xEu^{3+} samples, the lifetime of Tb^{3+} decreases with increasing Eu^{3+} concentrations, which are 2.89ms, 1.94ms, 1.55 ms, 1.12ms, 0.854ms, 0.594ms, 0.355ms, 0.261ms, 0.256ms, 0.165ms, respectively. The luminescence lifetime of Tb^{3+} decreases with increasing Eu^{3+} concentration as reported by Zhang et al.,[55] Nazarov et al.[56] and Mueller et al.[57] The lifetimes diminished obviously further confirmed that there was energy transfer between Tb^{3+} and Eu^{3+}. In addition, the energy transfer efficiency from Tb^{3+} to Eu^{3+} was also investigated. Generally, the energy transfer efficiency from a sensitizer to activator

can be expressed as the following equation[58-60]

$$\eta_T = 1 - \frac{\tau_S}{\tau_{S0}} \qquad (2)$$

because the energy absorbed by Tb^{3+} transferred to Eu^{3+}, which is strong evidence for the energy transfer from Tb^{3+} to Eu^{3+}, where η_T is the energy transfer efficiency and τ_{so} and τ_s are the lifetimes of a sensitizer in the absence and presence of an activator, respectively.[61] In the $YPO_4 \cdot 0.8H_2O$: $0.04Tb^{3+}$, xEu^{3+} systems, Tb^{3+} is the sensitizer and Eu^{3+} is the activator. According to the above equation, the maximum energy transfer efficiency is 94.31% for x=0.18 shown in Figure 14. These high efficiencies of energy transfer primarily originate from the significant spectral overlap between Tb^{3+} emission bands and Eu^{3+} absorption bands, and the energy transfer may occur easily. It depends on the average distance (R) between the Tb^{3+} donor and Eu^{3+} acceptor ions. Exchange interaction generally requires an overlap of the donor and acceptor orbitals and an R value of less than 0.3-0.4 nm; otherwise, the electric multipole interaction may dominate.[62]

In order to examine the nature of energy transfer, the Van Uitert's formula[63,64] can be expressed by:

$$\log\left(\frac{I_0 - I}{I}\right) = \log\beta + \left(\frac{\theta}{3}\right)\log\left(\frac{C_\alpha}{C_0}\right) \qquad (3)$$

where I_0 and I are the intensity of the donor fluorescence in the absence and presence of the acceptor respectively, β is a parameter representing the strength of the multipolar interaction and θ is the separation exponent corresponding to the interaction, C_α is the concentration of the acceptor (Eu^{3+}) and C_0 is the concentration of the acceptor (Eu^{3+}) at which the emission intensity of donor (Tb^{3+}) is quenched to

50% of its original value. θ takes values of 6, 8 or 10 for dipole-dipole, dipole-quadrupole or quadrupole-quadrupole interactions, respectively. We have estimated C_0 to be 4.3 at.% and the corresponding plot is shown in Figure 15, in which slope (θ/3) is estimated to be 1.997 suggesting that the energy transfer mechanism from the Tb^{3+} to Eu^{3+} ions is an electric dipole-dipole interaction.

Due to energy transfer from Tb^{3+} to Eu^{3+} ions, the relative intensity of red-light emission of Eu^{3+} gradually increases corresponding to the decrease of green-emission of Tb^{3+}. The undoped $YPO_4 \cdot 0.8H_2O$ nanocrystals show a strong self-activated blue emission centered at 400 nm, which implies the emission color can be effectively tuned by controlling the Eu concentration. As displayed in Figure 16, points a (0.236, 0.411), b (0.234, 0.324), c (0.241, 0.252) and d (0.269, 0.278) denote the change trend in the chromatic coordination for different concentrations of Eu^{3+} ions, which can be effectively tuned to white light by changing the Eu^{3+} concentrations. The emission of $YPO_4 \cdot 0.8H_2O$: $0.04Tb^{3+}$, xEu^{3+} nanocrystals upon excitation at 380nm covers the visible-light range with a balance of red (592 nm), green (543 nm) and blue (400 nm) resulting in a white-light emission. This merit of tunable white-light emission makes the materials have potential applications in the fields of labeling, sensing, biomedicine, and color display. Moreover, the novel strategy of combination of self-activated and rare earth ions emissions might serve as guidance for the design and fabrication other microscaled inorganic materials with white light emission and tunable luminescent properties.

4. Conclusions

In conclusion, via a simple hydrothermal route, we demonstrated a controlled synthesis of orthophosphate nanocrystals using **Cit^{3-}** as a "shape modifier". The pH value plays a crucial role in obtaining $YPO_4 \cdot 0.8H_2O$ samples with various morphologies and a crystallization pH value of 6 was optimal. Meanwhile, a strong blue emission peaking at about 400 nm in $YPO_4 \cdot 0.8H_2O$ nanocrystals was observed at room temperature due to the employment of Cit^{3-}. The $CO_2^{\cdot-}$ radicals in the interstitials of the orthophosphate lattice might be responsible for the self-activated luminescence. Through the analysis of spectra of the $YPO_4 \cdot 0.8H_2O$: Tb^{3+}, Eu^{3+}, there existed effective energy transfer between Tb^{3+} and Eu^{3+}. Then, by controlling the doping concentration of Eu^{3+}, the luminescent color could be modified from green, blue, white easily due to different composition of emissions of Eu^{3+} resulted from different energy efficiency at different doping concentrations. Moreover, the energy transfer mechanism was proven to be dipole-dipole interaction. It can be concluded that **Cit^{3-}** as a template plays an indispensable role in limiting the agglomeration of particles, controlling the size of crystal particles and strong blue luminescent of the samples. The suitable excitation wavelength, regular shape and strong luminescence will make $YPO_4 \cdot 0.8H_2O$: Tb^{3+}, Eu^{3+} samples become superior candidates in UV LEDs.

Acknowledgments

This work was supported by the Science and Technology Development Planning Project of Jilin Province (20130522173JH), partially sponsored by China Postdoctoral Science Foundation, supported by National Found for

Fostering Talents of Basic Science (NO. J1103202) and by the Chunmiao Talents of Jilin Province.

†Electronic Supplementary Information (ESI) available: additional graphics as described in the text. See DOI: 10.1039/b000000x/

References

1. X. F. Li, J. D. Budai, F. Liu, J. Y. Howe, J. H. Zhang, X. J. Wang, Z. J. Gu, C. J. Sun, R. S. Meltzer and Z. W. Pan, *Light: Science & Applications,* 2013, **2,** e50-e57.
2. M. M. Shang, G. G. Li, D. L. Geng, D. M. Yang, X. J. Kang, Y. Zhang, H. Z. Lian , J. Lin, *J. Phys. Chem. C*, 2012, **116**, 10222-10231.
3. E. Matioli, S. Brinkley, K. M. Kelchner, Y. L. Hu, S. Nakamura, S. DenBaars, J. Speck, C. Weisbuch, *Light: Science & Applications,* 2012, **1,** e22-e28.
4. A. A. Setlur, W. J. Heward, Y. Gao, A. M. Srivastava, R. G. Chandran, R. G. M. V. Shankar, *Chem. Mater.*, 2006, **18**, 3314-3322.
5. J. Limpert, F. Stutzki, F. Jansen, H. J. Otto, T. Eidam, C. Jauregu, A. Tünnermann, *Light: Science & Applications,* 2012, **1**, e8-e12.
6. S. X. Yan, J. H. Zhang, X. Zhang, S. Z. Lu, X. G. Ren, Z. G. Nie , X. J. Wang, *J. Phys. Chem. C*, 2007, **111**, 13256-13260.
7. X. F. Fan, W. T. Zheng, D. J. Singh, *Light: Science & Applications,* 2014, **3**, e179-e192.
8. L. Manna, E. C. Scher, L. S. Li, A. P. Alivisatos., *J. A. Chem. Soc.*, 2002, **124**, 7136-7145.
9. X . Wang, Y. D. Li, *Angew. Chem. Int .Ed.*, 2002, **41**, 4790-4173.
10. X. Wang, X. M. Sun, D. P. Yu, B. S. Zou, Y. D. Li., *Adv Mater*, 2003, **15**, 1442-1445.
11. X. Wang, Y. D. Li., *Chem. Eur. J.*, 2003, **9**, 5627-5635.
12. J. X. Zhu, Z. Gui, Y. Y. Ding. *Mater. Lett.*, 2008, **62**, 2373-2376.

13. S. Heer, O. Lehmann , M. Haase , H. U. Gudel. *Angew. Chem. Int. Ed.*, 2003, **42**, 3179-3182.

14. Z. Y. Huo, C. Chen, D.R. Chu, H. H. Li, Y. D. Li. *Chem. Eur J.*, 2007, **13**, 7708-7714.

15. H. X. Mai, Y. W. Zhang, L. D. Sun, C. H. Yan. *Chem. Mater.*, 2007, **19**, 4514-4522.

16. R. X. Yan, X. M. Sun, X. Wang, Q. Peng, Y. D. Li., *Chem. Eur. J.*, 2005, **11**, 2183-2195.

17. Y. P. Fang, A. W. Xu, R. Q. Song, H. X. Zhang, L. P. You, J. C. Yu, et al., *J. Am. Chem. Soc.*, 2003, **125**, 16025-16034.

18. Y. W. Zhang, Z. G. Yan, L. P. You, R. Si, C. H. Yan., *Eur. J. Inorg. Chem.*, 2003, **29**, 4099-4104.

19. L. X. Yu, D. C. Li, M. X. Yue., *Mater. Lett.*, 2007, **61**, 4374-4376.

20. H. Meyssamy, K. Riwotzki, A. Kornowski, S. Naused, M. Haase. *Adv. Mater.*, 1999, **11**, 840-844.

21. N. Banerjee, S. B. Krupanidhi, *Dalton Trans.*, 2010, **39**, 9789-9793.

22 J. Q. Hu, Q. Chen, Z. X. Xie, G. B. Han, R. H. Wang, B. Ren, Y. Zhang, Z. L. Yang, Z. Q. Tian, *Adv. Funct. Mater.*, 2004, **14**, 183-189.

23. Z. L. Fu, Z. J. Wu, D. Duan, X. H. Fu, *Dalton Trans.*, 2014, **43**, 2819-2827.

24. Q. Xie, Y. T. Qian, S. Y. Zhang, S. Q. Fu, W. C. Yu, *Eur. J. Inorg. Chem.* 2006, **2006**, 2454-2459.

25. U. Rambabu, N. R. Munirathnam, T. L. Prakash, S. Buddhudu, *Mater. Chem.*

Phys., 2002, **78**, 160-169.

26. K. Riwotzki, H. Meyssamy, H. Schnablegger, A. Kornowski, M. Haase., *Angew. Chem. Int. Ed.*, 2001, **40**, 573-576.

27. J. B. Liang, J. W. Liu, Q. Xie, S. Bai, W. C. Yu, Y. T. Qian, *J. Phys. Chem. B,* 2005, **109**, 9463-9467.

28. G. Bühler, C. Feldmann, *Chem. Int. Ed.*, 2006, **45**, 4864-4867.

29. C. M. Zhang, C. X. Li, S. S. Huang, Z. Y. Hou, Z. Y. Cheng, P. P. Yang, C. Peng, J. Lin, *Biomaterials*, 2010, 31, 3374–3383.

30. C. M. Zhang, S. S. Huang, D. M. Yang, X. J. Kang, M. M. Shang, C. Peng, J. Lin, *J. Mater. Chem.*, 2010, 20, 6674–668.

31. S. Angelov, R. Stoyanova, R. Dafinova, K. Kabasanov, K. *J. Phys.Chem. Solids*., 1986, 47, 409-412.

32 C. Zhang, J. Yang, Z. Quan, P. Yang, C. Li, Z. Hou and J. Lin, *Cryst. Growth Des.*, 2009, 9, 2725-2733.

33. C. Zhang, Z. Cheng, P. Yang, Z. Xu, C. Peng, G. Li, J. Lin, *Langmuir*, 2009, 25, 13591-13598.

34. C. K. Lin, C. M. Zhang, J. Lin, *J. Phys. Chem. C*, 2007, 111, 3300-3307.

35. B. E. Yoldas, *J. Mater. Res.*, 1990, 5, 1157-1158.

36. Z. Y. Li, W. M. Lam, C. Yang , B. Xu, G. X. Ni, S. A. Abbah, et al., *Biomaterials*, 2007, 28, 1452-1460.

37. H. Takeda, Y. Seki, S. Nakamura, K. Yamashita K. *J. Mater. Chem.*, 2002, 12, 2490-2495.

38. A. Doat, M. Fanjul, F. Pelle, E. Hollande, A. Lebugle, *Biomaterials*, 2003, 24,

3365-3371.

39. L. D. Carlos, R. A. Sa´ Ferreira, R. N. Pereira, M. Assunc, V. de Zea Bermudez, *J. Phys. Chem. B*, 2004, 108, 14924-14932.

40. C. M. Zhang , J. Lin, *Chem. Soc. Rev.*, 2012, 41, 7938-7961.

41. C. M. Zhang, C. K. Lin, C. X. Li, Z. W. Quan, X. M. Liu and J. Lin, *J. Phys. Chem. C*, 2008, 112, 2183-2192.

42. J. J. J. M. Donners, R. J. M. Nolte, N. A. J. M. Sommerdijk, *Adv. Mater.*, 2003, 15, 313-316.

43. M. H. Cao, C. W. Hu, Y. H. Wang, Y. H. Guo, C. X. Guo , E. B. Wang, *Chem. Commun.*, 2003, 15, 1884-1885.

44. H. Takeda, Y. Seki, S. Nakamura, K. Yamashita, *J. Mater. Chem.*, 2002, 12, 2490-2495.

45. C. M. Zhang, Z. Y. Cheng, P. P. Yang, Z. H. Xu, C. Peng, G. G. Li, J. Lin, *Langmuir*, 2009, 25, 13591-13598.

46. M. Shang, G. Li, X. Kang, D. Yang, D. Geng, C. Peng, Z. Cheng, H. Lian, J. Lin, *Dalton Trans.*, 2012, 41, 5571-5580.

47. M. Shang, D. Geng, X. Kang, D. Yang, Y. Zhang, J. Lin, *Inorg. Chem.*, 2012, 51, 11106-11116.

48. J. H. Huang, X. C. Wang, Y. D. Hou, X. F. Chen, L. Wu and X. Z. Fu, *Environ. Sci. Technol.*, 2008, 42, 7387-7391.

49. J. E. Shelby, *J. Am. Ceram. Soc.*, 1983, 66, 414-416.

50. Z. J. Zhang, H. H. Chena, X. X. Yang, J. T. Zhao, *Mater. Sci. Eng. B*, 2007, 145,

34-40,

51. J. Yang, C. M. Zhang, C. X. Li, Y. N. Yu, J. Lin, *Inorg. Chem.*, 2008, 47, 7262-7260.

52. X. L. Liang, Z. Y. Lin, Y. X. Yang, Z. W. Xing, G. R. Chen, *J. Am. Ceram. Soc.*, 2012, 95, 275-279.

53. Y. Tian, B. j. Chen, B. N. Tian, N. S. Yu, J. S. Sun, X. P. Li, J. S. Zhang, L. H. Cheng, H.Y. Zhong, Q. Y. Meng, R. N. Hua, *J. Colloid. Interf. Sci.*, 2013, 393, 44-52.

54. G. Blasse, B. C. Grabmarier, *Luminescent Materials, Sprinnger-Verlag,* 1994, 96.

55. Z. J. Zhang, H. H. Chena, X. X. Yang, J. T. Zhao, *Mate. Sci. Eng. B*, 2007, 145, 34-40.

56. M. V. Nazarov, D. Y. Jeon, J. H. Kang, E. J. Popovici, L. E. Muresan, *Solid State Commun.*, 2004, 131, 307-311.

57. A. H. Mueller, M. A. Petruska, M. Achermann, D. J. Werder, E. A. Akhadov, D. D. Koleske, M. A. Hoffbauer, V. I. Klimov, *Nano. Lett.*, 2005, 5, 1039-1044.

58. G. A. Kumar, P. R. Biju, G. Jose, N. V. Unnikrishnan, *Mater. Chem. Phys.*, 1999, 60, 247-255.

59. P. I. Paulose, G. Jose, V. Thomas, N. V. Unnikrishnan, M. K. R. Warrier, *J. Phys. Chem. Solids.*, 2003, 64, 841-846.

60. S. Rai, S. Hazarika, *Opt. Mater.*, 2008, 30, 1343-1348.

61. M. M. Shang, G. G. Li, X. J. Kang, D. M. Yang, D. L. Geng, J. Lin, *ACS. Appl.*

Mater. Inter., 2011, 3, 2738-2746.

62. D. L. Dexter and J. H. Schulman, *Chem. Phys.*, 1954, 22, 1063-1070.

63. L. G. Van Uitert, *Proc. Int. Conf. Lumin.*, 1966, 1588.

64. L. G. Van Uitert, E. F. Dearborn and J. J. Rubin, *J. Chem. Phys.*, 1966, 45, 1578-1584.

Figure Captions

Figure 1: XRD powder patterns of $YPO_4 \cdot 0.8H_2O$ nanocrystals prepared by hydrothermal method at 180°C for 24h at (a) pH = 6; (b) pH = 7; (c) pH = 8; (d) pH = 9 (e) pH = 10; (f) pH = 11; (g) pH = 12.

Figure 2: XRD powder patterns of the $YPO_4 \cdot 0.8H_2O$ with different rare earth ions. (a) $YPO_4 \cdot 0.8H_2O$; (b) $YPO_4 \cdot 0.8H_2O$: Tb^{3+} ; (c) $YPO_4 \cdot 0.8H_2O$: Eu^{3+} ; (d) $YPO_4 \cdot 0.8H_2O$: Eu^{3+}, Tb^{3+}. These samples were prepared under the similar conditions. The standard data for $YPO_4 \cdot 0.8H_2O$ (JCPDS card no. 42-0082) was shown as reference.

Figure 3: The FE-SEM (a, b) pH=6; (c, d) pH=11, TEM (e, PH=6) and HR-TEM (f, PH=6) images of $YPO_4 \cdot 0.8H_2O$ samples.

Figure 4: The excitation and emission spectra of $YPO_4 \cdot 0.8H_2O$ nanocrystals prepared in the presence of trisodium citrate (dashed line is the emission spectrum of $YPO_4 \cdot 0.8H_2O$ nanocrystals prepared without trisodium citrate).

Figure 5: EPR spectra for (a) the luminescent $YPO_4 \cdot 0.8H_2O$ nanocrystals prepared with trisodium citrate and (b) the $YPO_4 \cdot 0.8H_2O$ nanocrystals obtained without trisodium citrate in the preparation process.

Figure 6: FT-IR spectra for $YPO_4 \cdot 0.8H_2O$ prepared with trisodium citrate (a), $YPO_4 \cdot 0.8H_2O$ in the absence of trisodium citrate (b), respectively.

Figure 7: The excitation (λ_{em} = 545nm) and emission (λ_{ex} = 218nm) spectra of the $YPO_4 \cdot 0.8H_2O$: $0.04Tb^{3+}$ nanocrystals at room temperature.

Figure 8: The excitation (λ_{em} = 592nm) and emission (λ_{ex} = 395nm) spectra of the $YPO_4 \cdot 0.8H_2O$: $0.04Eu^{3+}$ nanocrystals at room temperature.

Figure 9: The emission (λ_{ex}=380nm) spectrum of the $Y_{0.92}PO_4 \cdot 0.8H_2O$: $0.04Tb^{3+}$, $0.06Eu^{3+}$ nanocrystals at room temperature.

Figure 10: The emission spectrum of the $Y_{0.96}PO_4 \cdot 0.8H_2O$: $0.04Tb^{3+}$ (the black line, λ_{ex}=218nm) and the excitation spectrum of $Y_{0.96}PO_4 \cdot 0.8H_2O$: $0.04Eu^{3+}$ (the red line, λ_{em}=592nm).

Figure 11: Emission spectra of the $Y_{0.96}PO_4 \cdot 0.8H_2O$:$0.04Tb^{3+}$ (black line), $Y_{0.94}PO_4 \cdot 0.8H_2O$:$0.04Tb^{3+}$, $0.02Eu^{3+}$ (red line) and $Y_{0.92}PO_4 \cdot 0.8H_2O$:$0.04Tb^{3+}$, $0.04Eu^{3+}$ (blue line) nanocrystals under the excitation at 486nm laser light.

Figure 12: The emission spectra of the $Y_{0.96-x}PO_4 \cdot 0.8H_2O$: $0.04Tb^{3+}$, xEu^{3+} (λ_{ex}=380nm) nanocrystals with different Eu^{3+} concentrations.

Figure 13: Decay curve of Tb^{3+} emission transitions in the $Y_{(0.96-x)}PO_4 \cdot 0.8H_2O$: $0.04Tb^{3+}$, xEu^{3+} samples (x=0, 0.02, 0.04, 0.06, 0.08, 0.10, 0.12, 0.14) under the excitation at 486nm laser light.

Figure 14： The energy transfer efficiency Tb^{3+} to Eu^{3+} in $Y_{0.96-x}PO_4 \cdot 0.8H_2O$: $0.04Tb^{3+}$, xEu^{3+} samples (x=0.02, 0.04, 0.06, 0.08, 0.10, 0.12, 0.14, 0.16, 0.18) under the excitation at 486nm laser light.

Figure 15: Plot of intensity variation of Tb^{3+} fluorescence, with Eu^{3+} concentration in relation to Van Uitert's formula.

Figure 16： CIE chromaticity diagram of the samples $Y_{0.96-x}PO_4 \cdot 0.8H_2O$: $0.04Tb^{3+}$, xEu^{3+} for different concentrations of Eu^{3+} doping: (a) x=0; (b) x=0.02; (c) x=0.12 and (d) x=0.18 under the excitation at 380nm.

Figure S1: The emission spectra of the $YPO_4 \cdot 0.8H_2O$ (black line), $YPO_4 \cdot 0.8H_2O$:

$0.04Eu^{3+}$ (red line), $YPO_4 \cdot 0.8H_2O$:$0.04La^{3+}$ (blue line) and $YPO_4 \cdot 0.8H_2O$: $0.04Tb^{3+}$ (magenta line) under the excitation at 380nm.

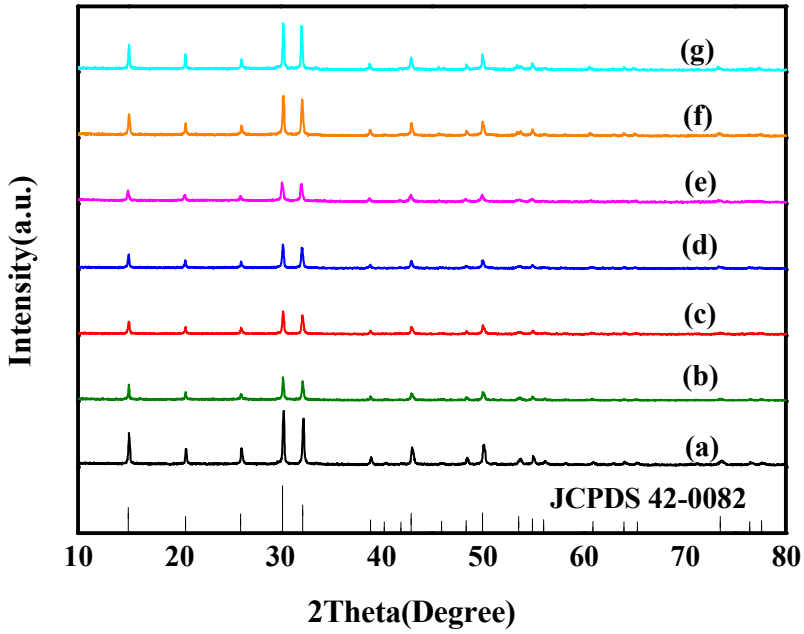

Figure 1: XRD powder patterns of $YPO_4 \cdot 0.8H_2O$ nanocrystals prepared by hydrothermal method at 180°C for 24h at (a) pH = 6; (b) pH = 7; (c) pH = 8; (d) pH = 9 (e) pH = 10; (f) pH = 11; (g) pH = 12.

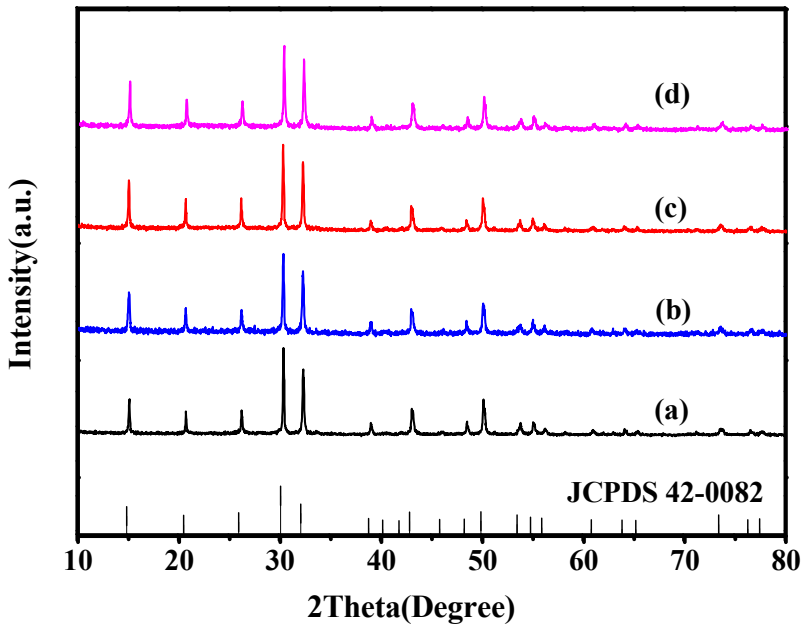

Figure 2: XRD powder patterns of the $YPO_4 \cdot 0.8H_2O$ with different rare earth ions. (a) $YPO_4 \cdot 0.8H_2O$; (b) $YPO_4 \cdot 0.8H_2O$: Tb^{3+} ; (c) $YPO_4 \cdot 0.8H_2O$: Eu^{3+} ; (d) $YPO_4 \cdot 0.8H_2O$: Eu^{3+}, Tb^{3+}. These samples were prepared under the similar conditions. The standard data for $YPO_4 \cdot 0.8H_2O$ (JCPDS card no. 42-0082) was shown as reference.

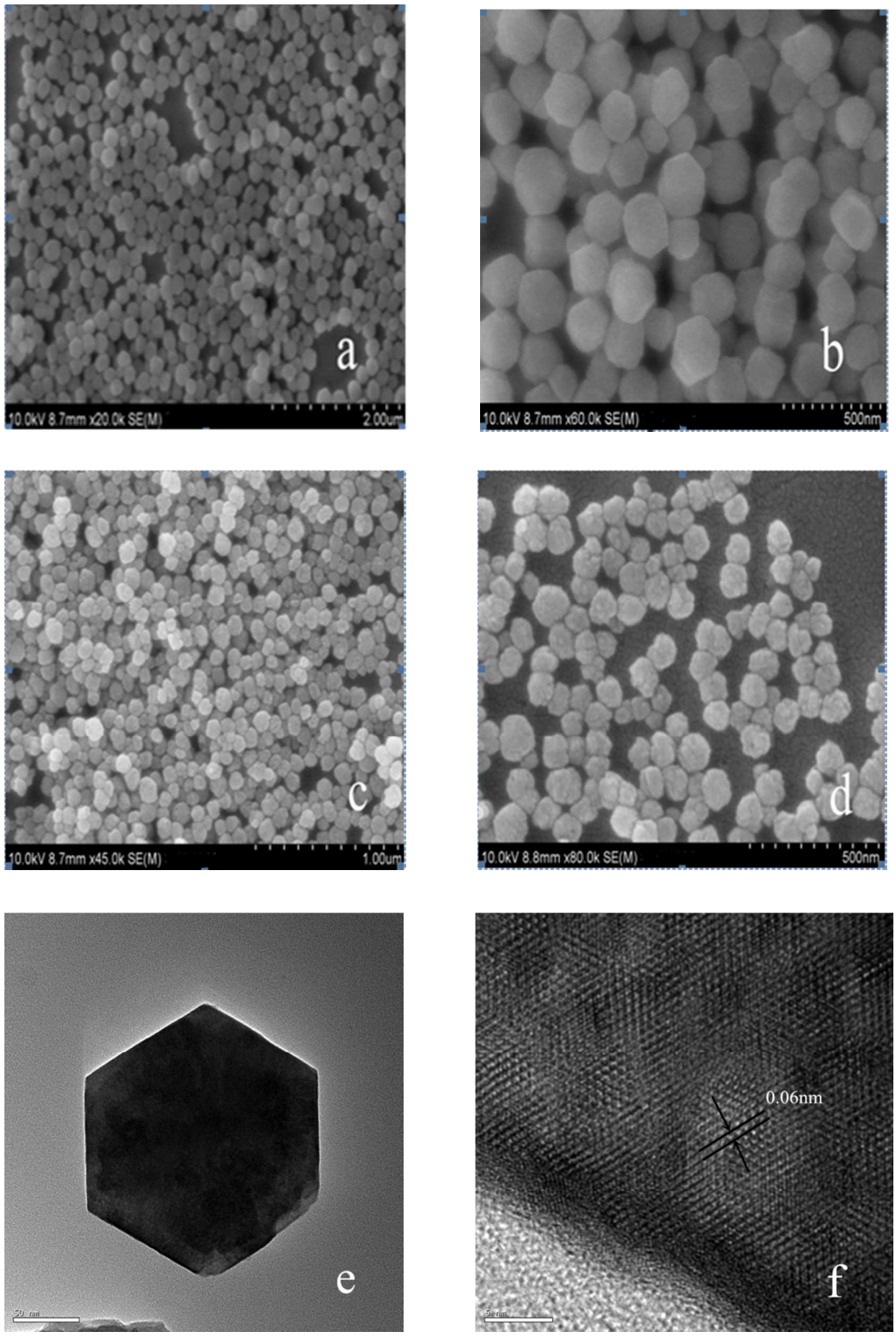

Figure 3: The FE-SEM (a, b) pH=6; (c, d) pH=11, TEM (e, PH=6) and HR-TEM (f, PH=6) images of $YPO_4 \cdot 0.8H_2O$ samples.

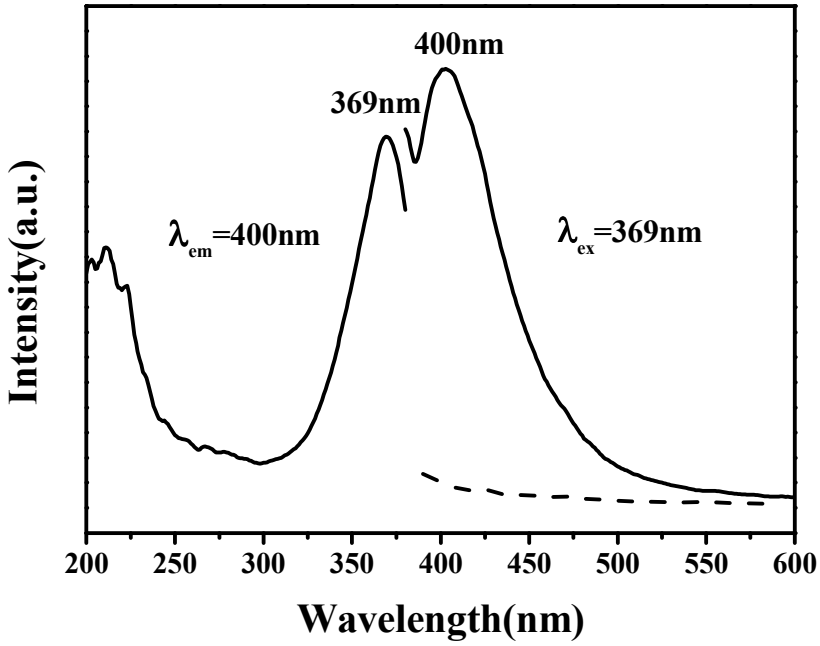

Figure 4: The excitation and emission spectra of $YPO_4 \cdot 0.8H_2O$ nanocrystals prepared in the presence of trisodium citrate (dashed line is the emission spectrum of $YPO_4 \cdot 0.8H_2O$ nanocrystals prepared without trisodium citrate).

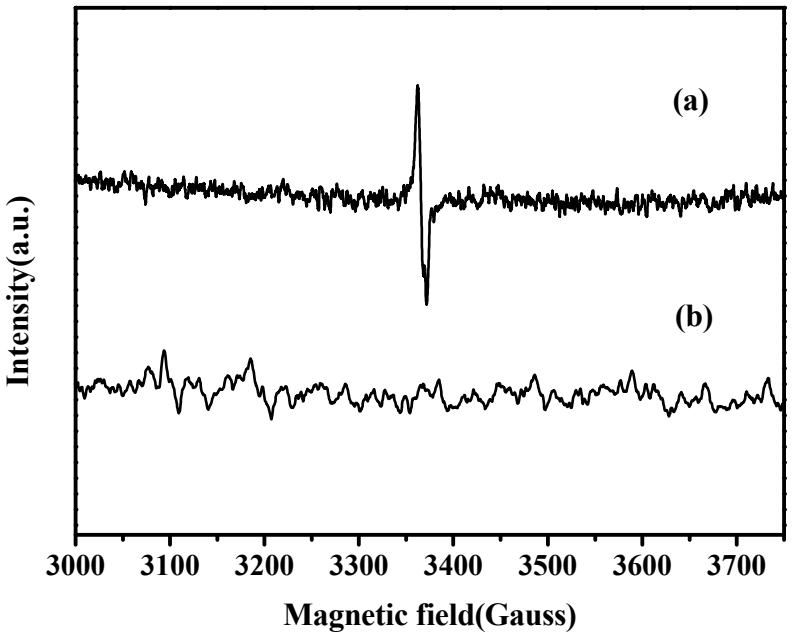

Figure 5: EPR spectra for (a) the luminescent $YPO_4 \cdot 0.8H_2O$ nanocrystals prepared with trisodium citrate and (b) the $YPO_4 \cdot 0.8H_2O$ nanocrystals obtained without trisodium citrate in the preparation process.

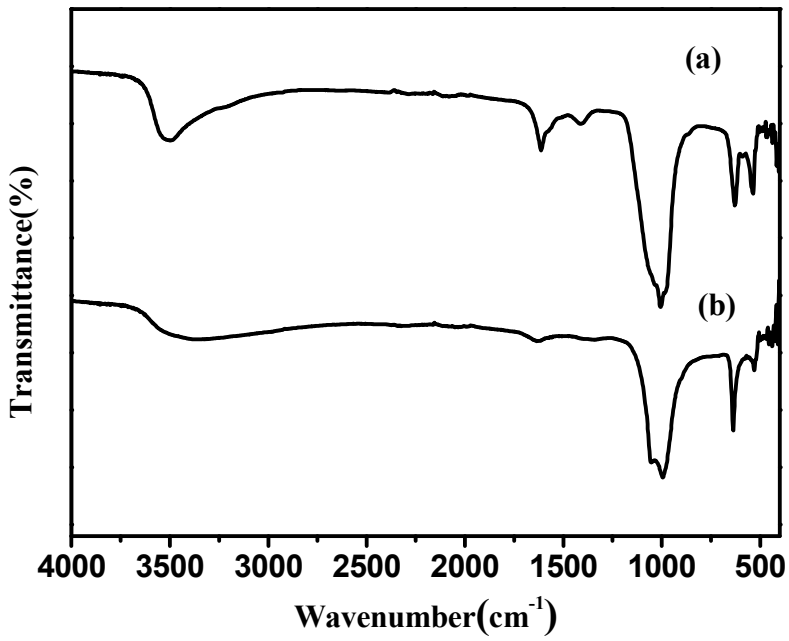

Figure 6: FT-IR spectra for $YPO_4 \cdot 0.8H_2O$ prepared with trisodium citrate (a), $YPO_4 \cdot 0.8H_2O$ in the absence of trisodium citrate (b), respectively.

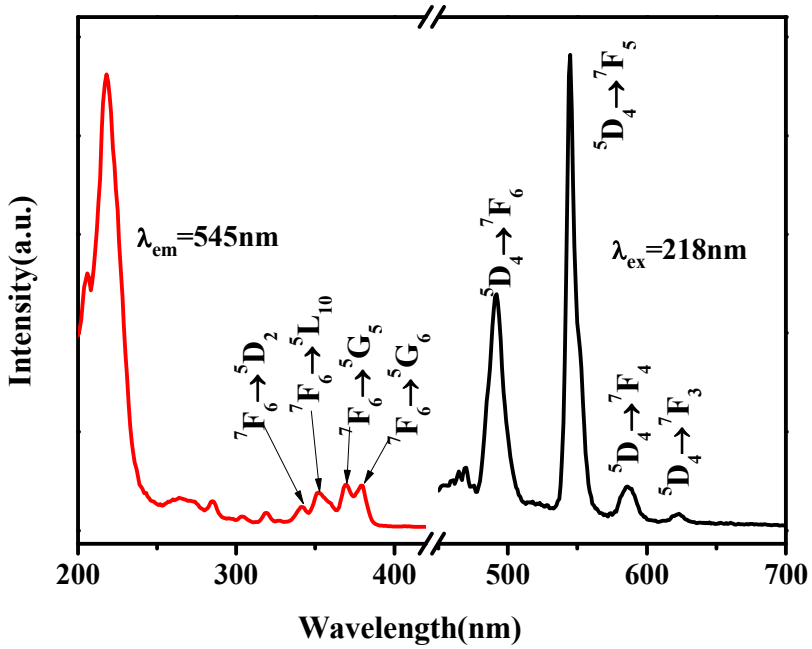

Figure 7: The excitation (λ_{em} = 545nm) and emission (λ_{ex} = 218nm) spectra of the $YPO_4 \cdot 0.8H_2O$: $0.04Tb^{3+}$ nanocrystals at room temperature.

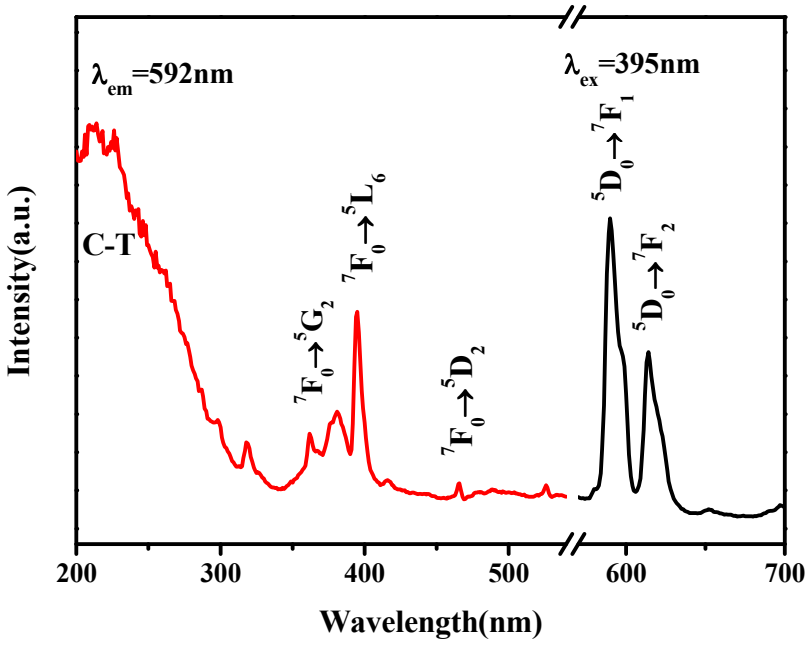

Figure 8: The excitation (λ_{em} = 592nm) and emission (λ_{ex} = 395nm) spectra of the $YPO_4 \cdot 0.8H_2O$: $0.04Eu^{3+}$ nanocrystals at room temperature.

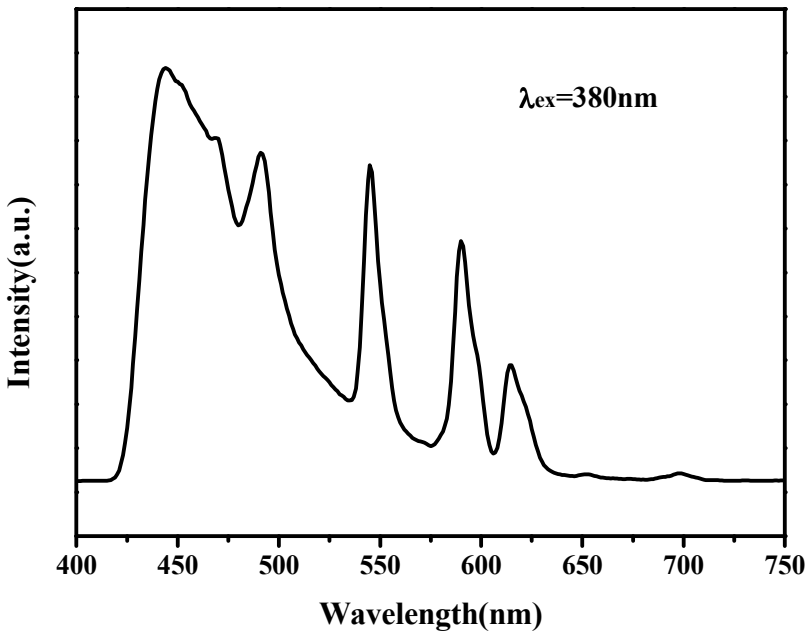

Figure 9: The emission (λ_{ex}=380nm) spectrum of the $Y_{0.92}PO_4 \cdot 0.8H_2O$: $0.04Tb^{3+}$, $0.06Eu^{3+}$ nanocrystals at room temperature.

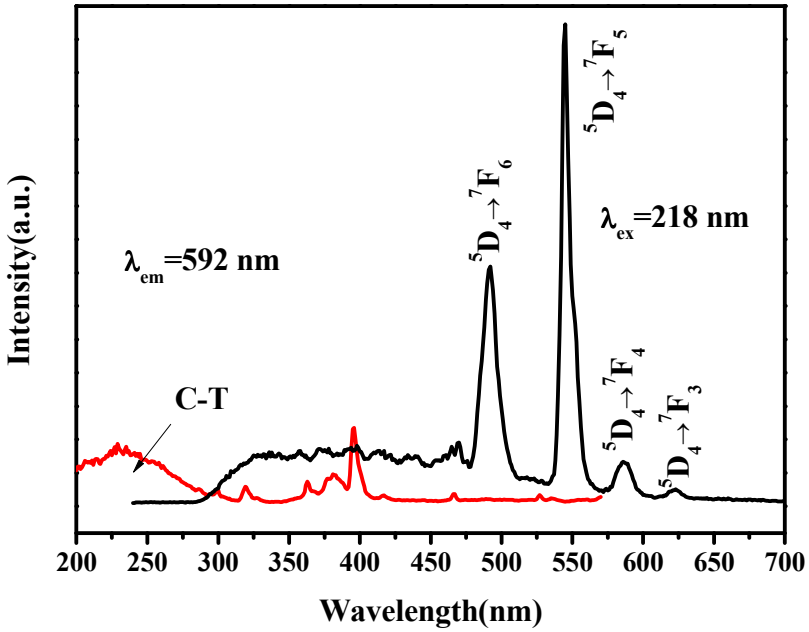

Figure 10: The emission spectrum of the $Y_{0.96}PO_4 \cdot 0.8H_2O$: $0.04Tb^{3+}$ (the black line, λ_{ex}=218nm) and the excitation spectrum of $Y_{0.96}PO_4 \cdot 0.8H_2O$: $0.04Eu^{3+}$ (the red line, λ_{em}=592nm).

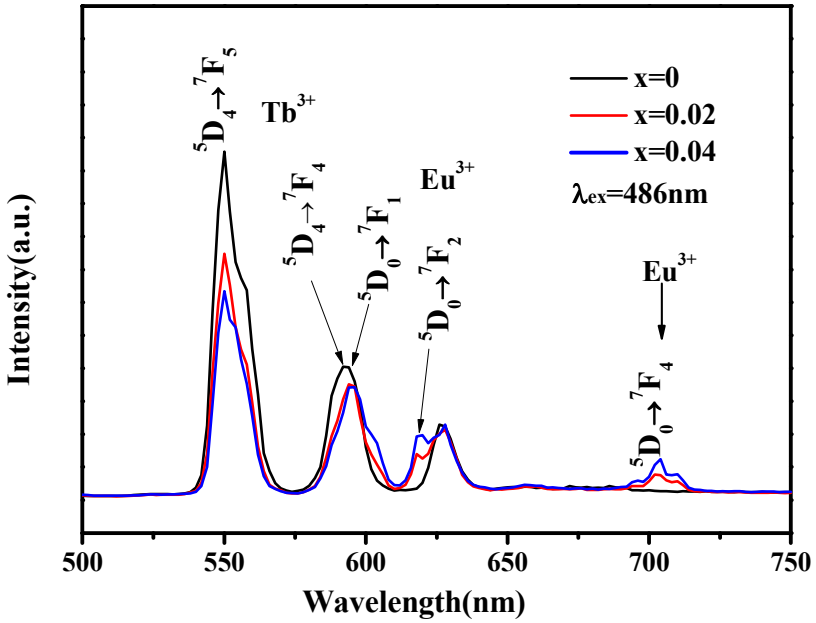

Figure 11: Emission spectra of the $Y_{0.96}PO_4 \cdot 0.8H_2O{:}0.04Tb^{3+}$ (black line), $Y_{0.94}PO_4 \cdot 0.8H_2O{:}0.04Tb^{3+}$, $0.02Eu^{3+}$ (red line) and $Y_{0.92}PO_4 \cdot 0.8H_2O{:}0.04Tb^{3+}$, $0.04Eu^{3+}$ (blue line) nanocrystals under the excitation at 486nm laser light.

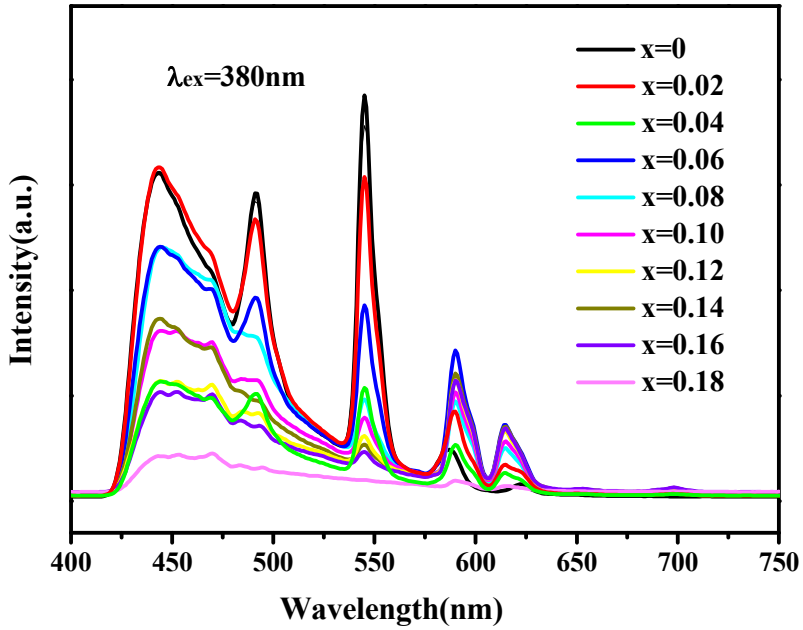

Figure 12: The emission spectra of the $Y_{0.96-x}PO_4 \cdot 0.8H_2O$: $0.04Tb^{3+}$, xEu^{3+} (λ_{ex}=380nm) nanocrystals with different Eu^{3+} concentrations.

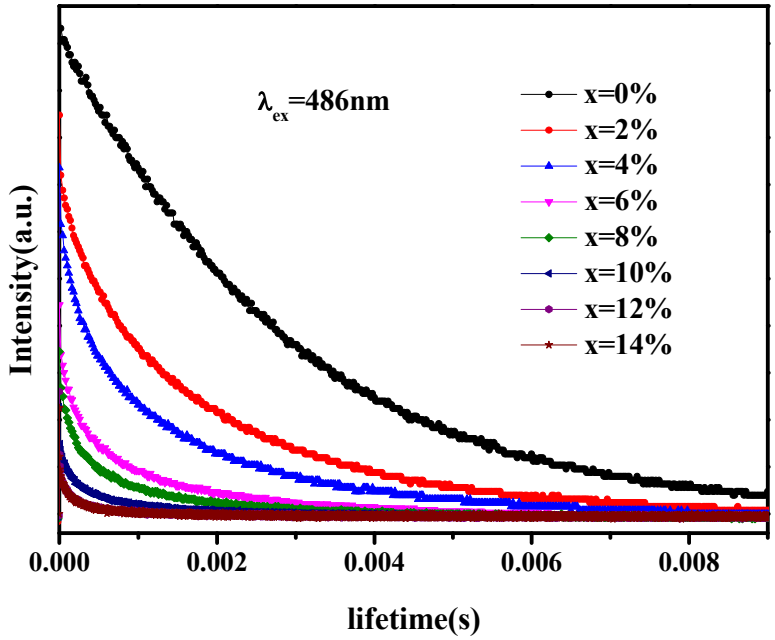

Figure 13: Decay curve of Tb^{3+} emission transitions in the $Y_{(0.96-x)}PO_4 \cdot 0.8H_2O$: $0.04Tb^{3+}$, xEu^{3+} samples (x=0, 0.02, 0.04, 0.06, 0.08, 0.10, 0.12, 0.14) under the excitation at 486nm laser light.

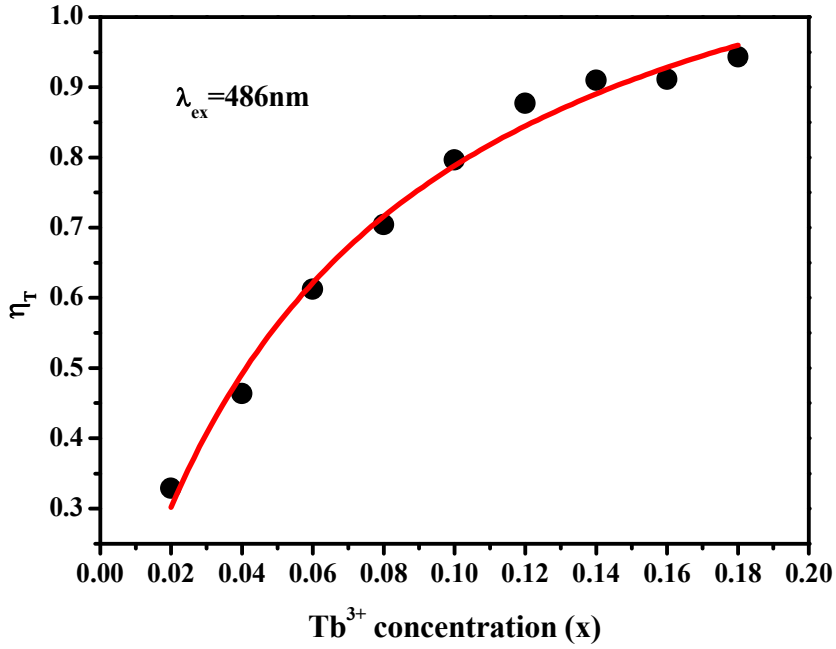

Figure 14： The energy transfer efficiency Tb^{3+} to Eu^{3+} in $Y_{0.96-x}PO_4 \cdot 0.8H_2O$: $0.04Tb^{3+}$, xEu^{3+} samples (x=0.02, 0.04, 0.06, 0.08, 0.10, 0.12, 0.14, 0.16, 0.18) under the excitation at 486nm laser light.

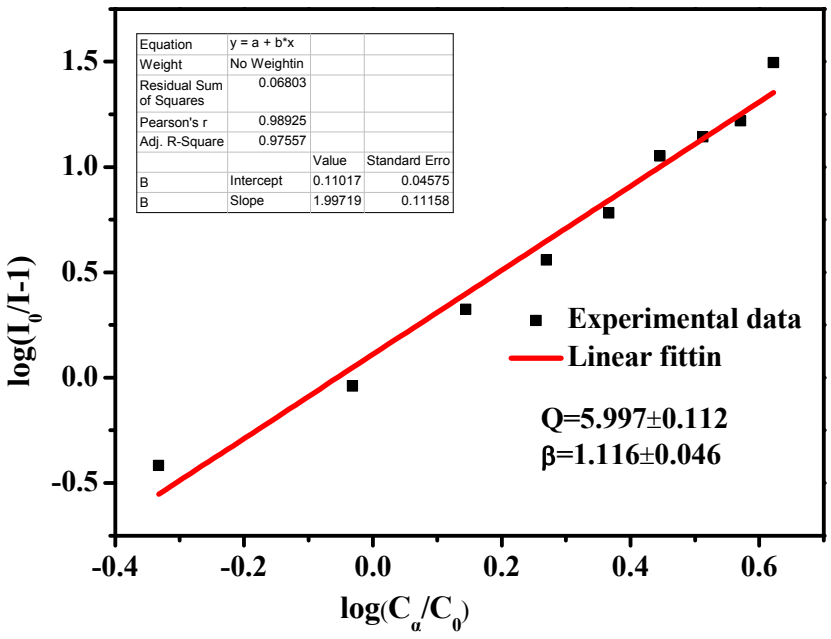

Figure 15: Plot of intensity variation of Tb^{3+} fluorescence, with Eu^{3+} concentration in relation to Van Uitert's formula.

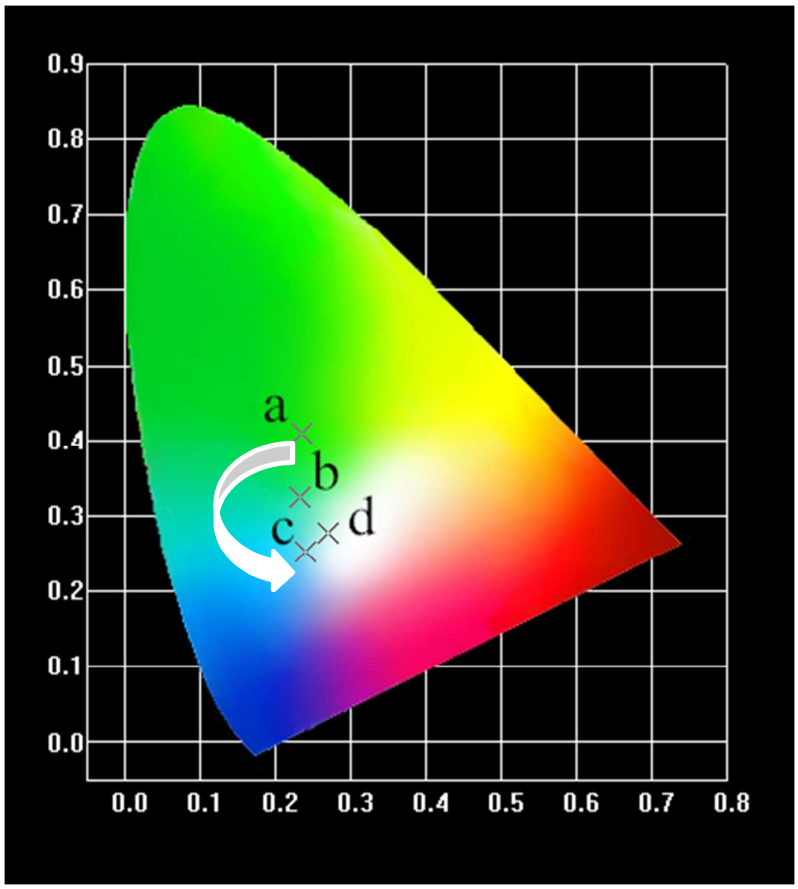

Figure 16: CIE chromaticity diagram of the samples $Y_{0.96-x}PO_4 \cdot 0.8H_2O$: $0.04Tb^{3+}$, xEu^{3+} for different concentrations of Eu^{3+} doping: (a) x=0; (b) x=0.02; (c) x=0.12 and (d) x=0.18 under the excitation at 380nm.

A table of contents entry

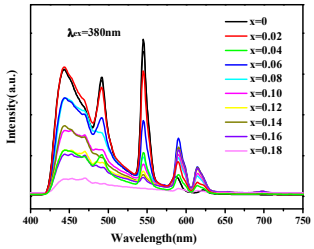

The emission spectra of $Y_{0.96-x}PO_4 \cdot 0.8H_2O$: $0.04Tb^{3+}$, xEu^{3+} (x=0~0.18) nanocrystals could result in tunable emission with self-activated luminescence and rare earth-doping emission.